Shape-changing Robotic Mannequin Shoulder with Bio-inspired Layered Structure

Juncai Long, *Student Member, IEEE,* Jituo Li, Yiwen Lu, Chengdi Zhou, Guodong Lu, Yixiong Feng

***Abstract*— Shape-changing robotic mannequin is a humanoid robot for imitating shapes of human bodies. The diversity of human bodies makes it difficult to imitate various body shapes, especially the shoulders. This paper proposes a rigid-flexible-soft coupling three-layered robotic mannequin shoulder inspired by human body anatomy. The robotic mannequin can adjust the anisotropic deformation of its human-like skin to imitate body dimensions, shape details and surface curvatures of target bodies. Structurally, the inner skeleton layer is composed of rigid framework and linear actuators for changing the global body dimensions. The middle muscle layer consists of flexible patches and layer-jamming bars with tunable stiffness for controlling the surface curvatures. The outer soft skin layer envelops the patches, forming a human-like surface of the robotic mannequin. To imitate a human body, the linear actuators drive the patches forward, which deforms the elastic skin layer. The tensioned skin layer inversely drives the bending deformation of patches, which can be controlled by layer-jamming bars. We design the three-layered structure by analyzing the shape differences of hundreds of scanned human models. An energy-based method is proposed to predict and control the coupling deformation of the layered structure. A physical robotic shoulder prototype has been built to verify the effectiveness of our method.**

I. Introduction

ROBOTIC mannequin is a mechatronic device designed to imitate shapes of different human bodies, which can be potentially used in remote tailoring and online garment selling. Dressing effects of a ready-made garment on different human bodies can be obtained by putting the garment on the robot and driving the robot to imitate target human bodies. Customers can get realistic dressing effects without having to try on the clothes in person. However, designing such a robotic mannequin is challenging. Mechanically, the very limited space inside the robot makes it difficult to accommodate complex structure and many drives. Geometrically, shapes of human bodies differ in both body dimensions and surface Gaussian curvatures. To imitate different body shapes, controllable tension and bidirectional bending are required for the surface of the robotic mannequin, which is obviously not easy. Most of the existing methods simplify this problem by discretization, i.e., dividing the robotic mannequin surface into patches [1], [2], [5], as illustrated in Fig. 1(a), Fig. 1(b) and Fig. 1(c), respectively. Dimensions of the robotic mannequins are controlled by adjusting gap sizes between adjacent patches. Tensile deformation is simplified as unidirectional bending, which however cannot adjust the local surface Gaussian curvatures. The latest work done by Tian et al.[4] goes a long way toward achieving curvature-controlled shape imitation. They designed a soft robotic mannequin with elastic skin enveloping several air chambers, as shown in Fig. 1(d). By inflating the air chambers, the shape of elastic skin can be adjusted. Their approach focusses on the part under the shoulder, such as the thorax and the abdomen.

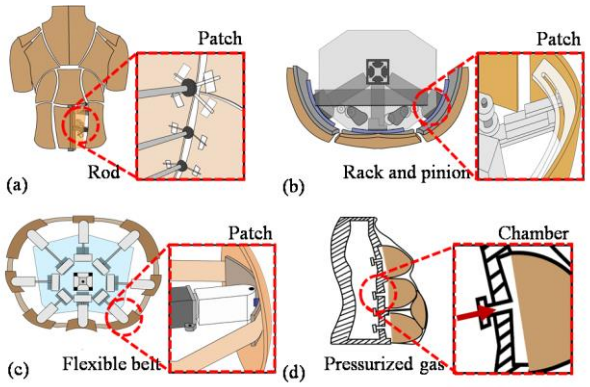

Figure. 1. Existing robotic mannequins. (a) Patch-based mannequin driven by rod [1]. (b) Patch-based mannequin driven by rack and pinion [2]. (c) Belt-based mannequin driven by elastic bar and flexible belt [3]. (d) Chamber-based mannequin driven by pressurized gas [4].

The shape of the shoulder is much more complex than other body parts and is affected by its adjacent areas. The shoulders, chest, neck, back and upper arms are the areas of the body that our robotic mannequin seeks to model, as shown in Fig. 2(a). Referring to the anthropometric definitions and methods for garment [6], [7], [8], we use shoulder width ①, shoulder slope ②, arm circumference ③, shoulder thickness ④, and neck circumference ⑤ to describe the deformability of the robotic mannequin shoulder.

A. Related works

1) Shape-changing robotic mannequin

As shown in Fig. 1, the existing shape-changing robotic mannequins can be roughly divided into three categories according to their deformation forms.

This work was supported in part by the National Natural Science Foundation of China under Grant No. 52275276 and in part by the Research Funding of Zhejiang University Robotics Institute. *(Corresponding author: Jituo Li)*.

The authors are with State Key Laboratory of Fluid Power and Mechatronic Systems, Zhejiang University, Hangzhou 310007, China. (Email: 12025082@zju.edu.cn; jituo_li@zju.edu.cn; yiwenlu@zju.edu.cn; 22025113@zju.edu.cn; lugd@mail.hz.zj.cn; fyxtv@zju.edu.cn).

The patch-based approaches [1], [2], [5] discretize the surfaces of robotic mannequins into several patches. The shapes of the robots are controlled by changing the positions of patches. Abels et al. [1] links adjacent patches with passive elastic bars, as shown in Fig. 1(a). The elastic bars cannot make patches produce controllable elastic deformation; therefore, the curvature of each patch can hardly be actively changed. The inability of controlling local Gaussian curvature is the common problem of the existing patch-based approaches.

Li et al. [3] proposed a belt-based robotic mannequin composed of flexible belts that are interwoven horizontally and longitudinally, as shown in Fig. 1(c). Each flexible belt envelops several elastic bars, whose bending can be controlled by the length of the flexible belt. Their approach can change the curvatures of elastic bars in a certain horizontal plane.

The chamber-based robotic mannequins [4], [9] use airtight airbags to shape elastic skin that envelops the airbags. When filled with compressed gas, the airbags expand to imitate the change in body shapes. However, it lacks the mechanism to control the anisotropic deformation of a single chamber, which limits its shape detail imitating ability.

2) Virtual try-on technology

Virtual try-on technology simulates dressing effects of a garment on customers by computing the virtual deformation of a digital garment on a digital human body, either in form of 2D image or 3D graphics. Roughly the recent works can be classified into two categories: physics-based simulation and learning-based simulation.

In physics-based methods, 3D virtual garments [10], [11], [12] and 3D human bodies [10], [11] are generated first; then a 3D garment is put on a target 3D human model by customizing the garment shape to make it suitable to target human body [15], [16], [17]. Although great improvements have been made in these areas, it is still not easy to mimic the garment dressing effects in high reality, especially multi-material and multi-layered garment, such as evening dress.

Learning-based methods have shown tremendous potential in virtual try-on. They are good at generalizing to unseen 2D images or 3D models, and they are usually fast since training and optimization are performed offline. Estimation of human body shape is the key to virtual try-on. Regression has been performed for the human body with a parametric human model [18], [19] or a voxel based representation [20], [21]. Although the learning-based estimation [22], or optimization using differentiable physics [23] has been studied, correspondence between the fabric material and its digital model are not well understood.

B. Our approach

Our work aims to design a robotic mannequin with human-like skin to imitate different human bodies. The elastic skin is required to be displaced, bent and stretched to produce anisotropic deformation. To address this issue, we propose a rigid-flexible-soft coupling three-layered structure inspired by human anatomy, as shown in Fig. 2. The inner structure is the skeleton layer, it consists of a set of linear actuators fixed on a rigid moveable support. The skeleton layer can imitate the global dimensions of target human bodies by displacement. The middle muscle layer is composed of flexible patches with adjustable stiffness. The patches can imitate curved surfaces and shape details of different human bodies by bending. The outer skin layer envelops the patches, constructing a continuous soft surface of the robotic mannequin. To imitate a human body, the linear actuators drive the patches forward, which deforms the elastic skin layer. The tensioned skin inversely forces the patches to bend. By controlling linear actuators and the stiffness of patches, the anisotropic deformation of the skin layer can be adaptively adjusted. As a result, the robotic shoulder can reach a state of force equilibrium.

Compared with the existing robotic mannequins, each patch of the coupled three-layered structure can achieve a controllable elastic deformation with one linear actuator and one variable stiffness structure. By adjusting both the position and stiffness of the muscle layer, the anisotropic deformation of the skin layer can be controlled, enabling it to imitate more body parts and a lager range of body dimensions. Our method improves surface continuity of the robot and reduces dependence on the number of actuators.

Algorithmically, we computationally designed the shapes and distributions of the linear actuators, the patches and the skin by analyzing shape differences of hundreds of scanned human models. An energy-based model is established to predict the deformation results of the coupled layered structure.

As far as we know, it is the first time to propose a rigid-flexible-soft coupling three-layered structure to get a shape controllable physical interface. We have verified our approach by prototyping a robotic mannequin shoulder with 29 degrees of freedom. In summary, our approach has the following academic contributions:

- A novel three-layered structure composed of rigid, flexible and soft materials for a shape-changing robotic shoulder.
- A method for designing the three-layered structure based on hundreds of scanned human models.
- An energy-based method for predicting the deformation of the three-layered structure.

II. Design of Shape-changing Robotic Shoulder

A. Overview

Skeleton, muscle, and skin are the three elements that determine body shape. In anatomy, rigid human bones support other structures and form the basic framework, affecting height and shoulder width etc. The flexible muscle is attached to the skeleton, which determines the local contour of a human body. The elastic skin layer covers the muscles and bones, forming the texture of the continuous body surface. The bones, muscles, and skin have different materials, functions, and structures, as shown in Fig. 2(b). The movement of bones, the contraction and bending of muscles, and the stretching of skin cooperatively shape the appearance of a human body.

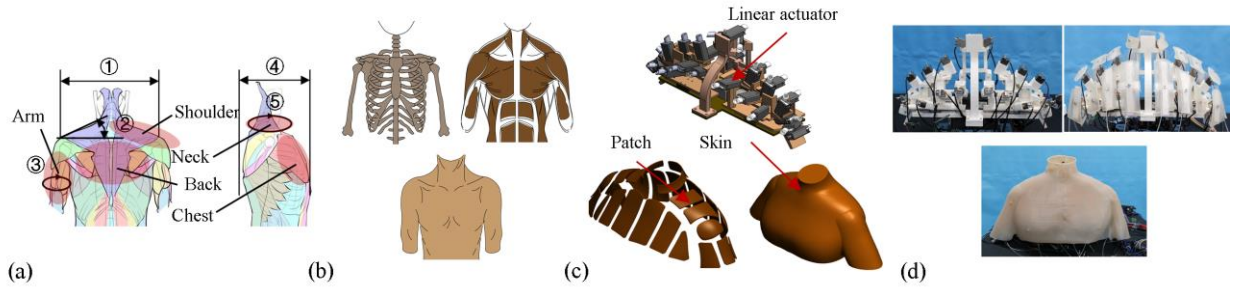

Figure. 2. Human anatomy-inspired design. (a) Areas of human body to imitate. (b) Human bones, muscle and skin. (c) Bio-inspired skeleton layer, muscle layer and skin layer of robotic mannequin shoulder. (d) The prototype.

Inspired by human anatomy, our robotic mannequin is designed as three layers correspondingly. The inner structure is rigid skeleton layer which is constructed with support framework and rigid linear actuators to support other structure and adjust shoulder width, as shown in Fig. 2(c). Two moveable platforms driven by stepper motors can slide to each side for changing shoulder width. The middle flexible muscle layer fixed on the skeleton layer is composed of flexible patches with adjustable stiffness, which is detailed in Section II.C. Skin layer is made of a hyperelastic membrane, and covers the muscle layer. In term of deformation principle, the three layers are coupled together. The motion of the rigid skeleton layer, the bending and variable stiffness of the flexible muscle layer, and the stretching of the skin layer combine to shape the appearance of the human body. When the linear actuators push the patches forward, the concentrated thrust forces transmit to the skin layer and turn to distributed forces. Consequently, the skin layer is stretched and its elastic potential energy encourages a tendency to shrink, which drives the patches to bend. As a result, the skin layer and the muscle layer reach a state of force equilibrium, i.e., the state of minimum elastic potential energy. We have fabricated a prototype shoulder to verify the design method, as shown in Fig. 2(d).

B. Design and decomposition of skin layer

The initial shape of our skin layer is obtained by averaging hundreds of 3D scanned human models obtained from [24], as shown in Fig. 3(a). Since the average skin shape represents the common features of most human bodies, the robot can imitate the body shapes of great majority of human bodies in the database within the limited deformation range. The robotic shoulder has a shoulder width of 322mm, a shoulder slope of 20°, a shoulder thickness of 195mm, a neck circumference of 310mm and an arm circumference of 291 mm. For fabrication and deformation simulation, the skin layer is modeled as a volumetric mesh. Methodologically, the skin surface is offset and discretized into a tetrahedral mesh by using the quality conforming Delaunay triangulation [25], as shown in Fig. 3(a)

The shape deformation from the initial state of the robot to a target shape can be regarded as a combination of stretching, rotating, and displacement. To make the layered structure compatible to these deformations, we first computed and decomposed the shape deformation of the skin layer; then corresponding actuators, other structures and materials are designed to support different kinds of deformations.

Considering the material of the skin layer is hyperelastic and isotropic, we use neo-hookean constitutive model [26] to describe the deformation. For the tetrahedral mesh of skin layer, the energy density inside each tetrahedron t_i is defined as

$$\Psi(I_1, J) = \frac{\mu}{2}(I_1 - 3) - \mu \log(J) + \frac{\lambda}{2}\log^2(J) \qquad (1)$$

where μ is the shear modulus. The invariants $I_1 = \mathrm{tr}(\mathbf{F}^T\mathbf{F})$ and $J = \det \mathbf{F}$. For incompressible materials we used, $J = 1$. $\mathbf{F}$ is deformation gradient tensor.

The stress-stretch relation [26] derived from (1) for curve fitting with uniaxial tensile testing data is

$$\sigma = \mu\left(\lambda^2 - \frac{1}{\lambda}\right) \qquad (2)$$

where, the stretch $\lambda = 1 + \varepsilon$. σ is the stress and ε is the strain.

μ can be determined by fitting uniaxial tensile curves with finite element simulation data, as shown in Fig. 3(b) and Fig. 3(c). The corresponding nominal stress-strain curves of the materials are shown in Fig. 3(d).

The deformation gradient tensor $\mathbf{F} \in \mathrm{R}^{3\times3}$ in (1) is

$$\mathbf{F} = \frac{\partial \vec{x}}{\partial \vec{X}} = \begin{pmatrix} x \\ y \\ z \end{pmatrix}\begin{pmatrix} \frac{\partial}{\partial X} & \frac{\partial}{\partial Y} & \frac{\partial}{\partial Z} \end{pmatrix} \qquad (3)$$

where $\vec{X} = \{X, Y, Z\}$ and $\vec{x} = \{x, y, z\}$ are the undeformed and deformed configuration for the three components. $\mathbf{F}$ is constant inside each tetrahedron.

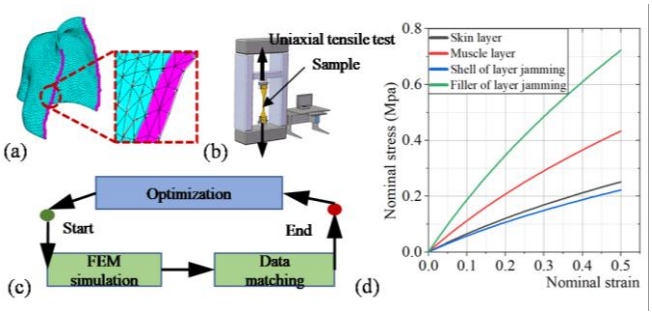

Figure. 3. Material models. (a) Tetrahedralized mesh. (b) Uniaxial tensile test. (c) Material coefficient optimization. (d) Constitutive models.

F contains rigid rotation and tensile deformation. Generally, adjacent areas on the skin layer have similar deformation gradient, according which we split the skin surface into patches. These patches form the muscle layer. Using the polar decomposition of $\mathbf{F} = \mathbf{RS}$, we get the rotation matrix **R** and scaling matrix **S**, which can be interpreted as the skin being first stretched by **S** and then rotated with **R**. The three eigenvalues of **S** (λ_1, λ_2 and λ_3) are the principal stretches and their corresponding eigenvectors give three orthogonal directions in the material coordinate system. As the stretching deformation is anisotropic, we designed layer-jamming structures attached to patches to actively change the local stiffness.

C. Design of muscle layer and variable stiffness structure

As shown in Fig. 4(a), the muscle layer is obtained by segmenting the skin layer. We first divided the skin layer into 5 parts, neck, shoulder, chest, back, upper arm, referring to the distribution of the main muscle groups in the shoulder area, such as the trapezius, deltoid, pectoralis major, etc. Then the shape differences between human bodies are analyzed. The areas with the greatest difference between human bodies are split into different patches for independent control. Areas with little shape difference between different human bodies are merged into the same patch for common control. The shape difference is obtained by analyzing the deformation gradient from the shape of the skin layer to the target human bodies shapes. For two adjacent tetrahedron with their deformation gradient $\mathbf{F}_i$ and $\mathbf{F}_j$, if $\|\mathbf{F}_i - \mathbf{F}_j\|_F^2 \leq \delta$, they are flagged as the same region, where δ is a threshold. For tetrahedron satisfying $\|\mathbf{F} - \mathrm{I}\|_F^2 \leq \delta$ or $\max(|\sigma_{\max} - 1|, |{\sigma_{\min}}^{-1} - 1|) \leq \delta$, it is considered a rigid part, where, $\sigma_{\max}$ and $\sigma_{\min}$ are the singular values of **F**. During clustering: (1) the areas with large deformation should be cut into discrete patches. (2) the areas with distinct deformation behaviors should be divided into different patches. Finally, 27 pieces of patches are obtained, and their boundaries are manually smoothed. The gap between two adjacent patches is 6 mm wide, as shown in Fig. 4(b). The change in arm circumference is achieved through the displacement of the three patches on the outside of the arm. The three patches can be moved forward, backward and laterally along the body to change the arm circumference.

To make the local stiffness of patches adjustable, a layer jamming structure is designed. As shown in Fig. 4(c), it consists of an airtight elastic shell connected with air tubes, and layers of inextensible material. In normal state, the friction between layers is small and it is easy for one layer to slip over another. The whole structure is easy to bend. When vacuumizing the shell, layers of paper are compressed together and the static friction between adjacent layers increases, which makes it difficult to slip in the interfaces between adjacent layers. The layers of paper are in a "jammed" state, and the whole structure is hard to bend and the local stiffness of patches increases. When the air pressure inside the shell restores to normal atmospheric pressure, the local stiffness of the patches accordingly decreases to the initial state. The distribution of the variable stiffness structure is shown in Fig. 4(d).

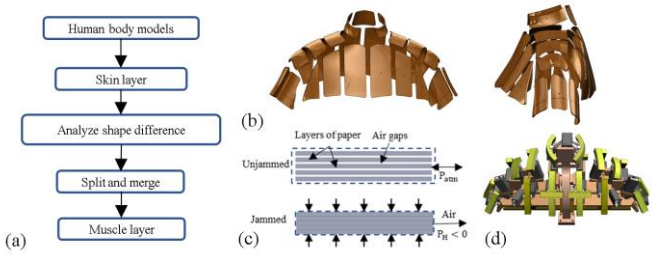

Figure. 4. Muscle layer design. (a) Design process for muscle layer. (b) Design results of muscle layer. (c) The two states of layer-jamming bar. (d) The distribution of layer-jamming bars.

Layer jamming structure is attached to patches. The non-stretchable conventional layer jamming structure hinders the original elastic deformation of patch, and cannot adjust the anisotropic deformation of patch by adjusting the tensile stiffness in different directions. Gauss' Theorema Egregium states that the Gaussian curvature of a surface is invariant under local isometry. In other words, the Gaussian curvature of a surface can be changed if one bends the surface with stretching it anisotropically. Therefore, the layer jamming element is designed as forked-finger structure, as shown in Fig. 5(c). The internal filling layers are crossed and connected to the elastic shell separately. When the structure is in jamming state, the bending stiffness and tensile stiffness both rapidly increase. As shown in Fig. 5(a) and Fig. 5(b), there are three states of the layer-jamming structure under the action of different magnitudes of external loads. The stiffness is maximum in the pre-slip stage, decreases in the partial-slip stage, and reaches the minimum in the full-slip phase.

Suppose that there are n overlapping rectangular layers in the layer jamming structure with layer thickness t, width w, and the coefficient of static friction is f_s, the vacuum pressure is P. The static friction limit is $f_s P$. The value of pressure decides the maximum bearing capacity of the structure.

For the tensile test, the maximum allowable shear stress is $\tau_{\max} = f_s P$, and the maximum allowable tensile force is $F_{shear} = \tau_{\max} A = f_s P n w l$, which scales linearly with overlapped area wl, P, n and f_s. The values of f_s under different states are measured by frictional experiments. For our forked-finger layer-jamming structure when unjammed, the tensile resistance is mainly the elasticity of the elastic shell. To compute the flexural rigidity when jammed, two cases are modelled as shown in Fig. 5(a). In the first case, layers can't slip between each other, and in the second case, layers are free to slip. The jammed layers behave as a single layer making the second moment of area I increase. For an unjammed structure,

$$I_{unjammed} = n\frac{wt^3}{12} \tag{4}$$

When jammed,

$$I_{jammed} = \frac{w(nt)^3}{12} \tag{5}$$

So that, $I_{jammed}/I_{unjammed} = n^2$, i.e., when jammed, the local bending stiffness of a patch can increase to n^2 times rapidly.

To verify the ability of the forked-finger type layer jamming structure, two orthogonal layer jamming structures are arranged to regulate the deformation of an elastic membrane, as shown in Fig. 5(d). Nonlinear quasi-static deformation of three-layered structure was simulated in soft ABAQUS/Standard, as shown in Figure 5(d). The square skin layer has a side length of 100mm and a thickness of 1mm with four edges fixed; the radius of the circular muscle layer is 35mm and the thickness is 1.5mm; the layer jamming has a length of 60mm and a width of 20mm. The materials of skin layer and patch are modeled as incompressible Neo-hookean model ($\mu = 0.23$Mpa for skin layer, $\mu = 0.41$Mpa for patch). The layer jamming was modeled as linear elastic materials (when unjammed $E = 7$Mpa, when jammed $E = 4$Gpa). For the simulation, a displacement of 20mm was applied to the inner surface of the layered-structure.

The dimensions and conditions of the experimental models match those of the FEA simulation. We applied vacuum pressure of -40kPa to orthogonal layer jamming structures in turn, and three different deformation results are generated. The deformation results were scanned using a 3D scanner and compared with the FEA simulation results. The errors are measured by Hausdorff distance, as shown in the second column of Figure 5(d). The results show that the layer jamming can effectively adjust the deformation of the layered structure, and the experimental results match the simulation results well.

D. Design and optimization of skeleton layer

One patch is controlled by one linear actuator. Accordingly, 24 linear actuators are assembled on the movable platforms and 3 linear actuators are fixed on the neck support, forming the skeleton layer, as shown in Fig. 6(a). Each platform can move along the left-right direction to imitate the shoulder width, which is controlled by stepper motors ①, motor support ② and screw-threaded flanges ③, as shown in Fig. 6(a). The connection relationships of the three layers are displayed in Fig. 6(b). The layer jamming bars are fixed to the rod of linear actuator and glued to the inner surface of patch. And the outer surface of the patch is adhered to the inner surface of skin layer.

Each patch is controlled by one fixed linear actuator. In order to improve the imitating effect for most people, we optimized the fixed pose of each linear actuator based on the transformation matrices between the initial state and target states of the corresponding patch. Let $\mathbf{P}_i = \{p_{i,1} \dots p_{i,j}\}$ and $\mathbf{Q}_i = \{q_{i,1} \dots q_{i,j}\}$ be the initial shape and target shape of ith patch P_i, where $p_{i,j}$ and $q_{i,j}$ are the paired jth point in the ith patch. The rigid transformation $\mathbf{M}_i = \{\mathbf{R}_i, \mathbf{t}_i\}$ between $\mathbf{P}_i$ and $\mathbf{Q}_i$ can be obtained by solving

$$(\mathbf{R}_i, \mathbf{t}_i) = \arg\min_{\mathbf{R} \in SO(3)} \sum_j \| \mathbf{q}_{i,j} - \mathbf{R}_i \mathbf{p}_{i,j} - \mathbf{t}_i \|^2 \qquad (6)$$

where $\mathbf{R}_i$ is the rotation matrix, and $\mathbf{t}_i$ is the translation matrix. $\mathbf{R}_i$ can be computed as

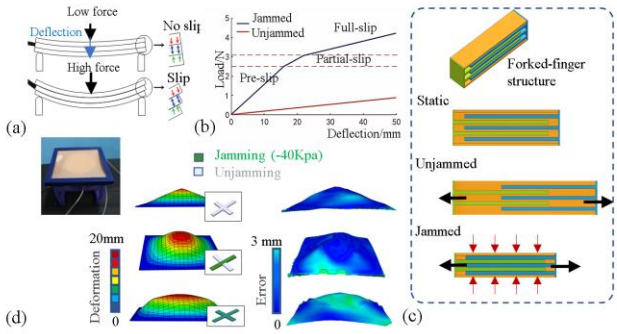

Figure. 5. Forked-finger layer jamming. (a) The states of layer jamming under different loads. (b) Three states of the layer-jamming. (c) The tensile properties of forked-finger layer jamming element. (d) Simulation and experiment results.

$$\mathbf{R}_i = \mathbf{V} \begin{bmatrix} 1 & 0 & 0 \\ 0 & 1 & 0 \\ 0 & 0 & d \end{bmatrix} \mathbf{U}^T \qquad (7)$$

where $d = \text{sign}(\det(\mathbf{P}_i \mathbf{Q}_i^T))$. V and $\mathbf{U}$ can be obtained by $\mathbf{P}_i \mathbf{Q}_i^T = \mathbf{U}\mathbf{\Sigma}\mathbf{V}^T$ with the singular value decomposition [27]. $\mathbf{t_i} = d_i \mathbf{e}_i$ contains the unit direction $\mathbf{e}_i$ and the value of displacement d_i. When $\mathbf{R}_i$ obtained, $\mathbf{t}_i = \bar{\mathbf{q}}_i - \mathbf{R}_i \bar{\mathbf{p}}_i$, where $\bar{\mathbf{p}}_i$ and $\bar{\mathbf{q}}_i$ are the centroids of patches.

When all the transformation matrices for different target shapes $S_1, \dots, S_k$ are obtained, the average rotation $\bar{\mathbf{R}}$ and the average displacement direction $\bar{\mathbf{t}}$ of each patch can be computed. The average rotation is

$$\bar{\mathbf{R}}_i = \arg\min_{\mathbf{R} \in SO(3)} \sum_{k=1}^{n} d\left(\mathbf{R}, \mathbf{R}_{i,k}\right)^2 \qquad (8)$$

where $\mathbf{R}_{i,k}$ is the rotation matrix of the ith patch to imitate the kth target shape. The distance of two rotations is defined as

$$d(\mathbf{R}_i, \mathbf{R}_j) = \frac{1}{\sqrt{2}} \| \log(\mathbf{R}_i^T \mathbf{R}_j) \| \qquad (9)$$

The average displacement direction $\bar{\mathbf{t}}_i$ is

$$\bar{\mathbf{t}}_i = \frac{\sum_{k=1}^{n} \mathbf{e}_k}{|\sum_{k=1}^{n} \mathbf{e}_k|} \qquad (10)$$

Each patch is assembled according to corresponding $\bar{\mathbf{t}}$ and $\bar{\mathbf{R}}$, as shown in Fig. 6(b). The control parameter d_i, i.e., the value of displacement d_i of each patch is recomputed as

$$d_i = (\bar{\mathbf{q}}_i - \bar{\mathbf{p}}_i) \cdot \bar{\mathbf{t}}_i \qquad (11)$$

E. Prototype fabrication

Sailner J300Plus printer with three base materials of significantly different stiffnesses: rigid RGD110T, soft FLX910T (30A), extra soft FLX920W (10A) is used to fabricate the robot. By mixing the three materials, we can print structures of shore hardness in 10A-90A. The hardness of the shell and the filling layers of the forked-finger actuator are 30A and 90A respectively. The shell and filler layers of the layer jamming are printed separately. After ultrasonic cleaning and UV secondary curing, we applied the soft FLX910T (30A) material as an adhesive to the connection

joint of the shell and filler and cured it using UV irradiation. The skeleton layer is printed with rigid material RGD110T. The hardness of patches is designed as 65A. For the skin layer, it is required to be stretched and bent to a large range to imitate human bodies. And when the external loading is removed, it can restore to rest shape. Thus, its material is selected as Dragon Skin 30 (Smooth-On Inc.) [26] which has good tensile properties and soft texture. The thickness of the skin layer is 1.5 mm. We designed the pouring mold and fabricated it through a FDM 3D printer.

The linear actuator is 40mm long, 20mm wide and 10mm high. It can feeds back the position of the push rod through a sliding potentiometer. The stroke of the motor is 0-20mm, and the maximum thrust is 30N.The inherent step angle of the stepper motor is 1.8°, and the holding torque output is 0.45Nm.

The measurement range of the tensile testing machine we used is 0-50N, the resolution of force is 0.001N, and the resolution of displacement is 0.01mm. The tensile tests were performed using a displacement-controlled loading mode at a constant test speed of 100mm/min.

Due to the working space of actuators, the shape simulation space of one robotic mannequin shoulder is impossible to cover the shape space of all human bodies. For our physical protype, the range of body dimensions that can be imitated is listed in Table I, which covers more than 50% human bodies according to the statistical data of Chinese adults [28]. For women, the coverage rate reaches 70%.

TABLE I. RANGE OF HUMAN BODY DIMENSIONS COVERED

Body part	Body size value (mm)	Percentage of people covered (male/female)
Neck circumference	310-420	\
Chest circumference	810-1040	60%/80%
Shoulder width	320-460	50%/70%
Shoulder thickness	190-230	55%/70%
Arm circumference	285-350	\
Shoulder slope	0°-35°	\

III. DEFORMATION PREDICTION

For simulation efficiency, we compute the deformation with Laplacian deformation [29] first to quickly approximate the deformation results, and then use finite element method [30] to improve the simulation accuracy. We combined the fast but inaccurate geometric deformation method with the slow but accurate finite element method to compensate for the shortcomings of a single simulation method.

A. Initializing skin deformation based on Laplacian method

When patches are displaced by the linear actuators, the deformed shape of the skin layer can be initialized through Laplacian mesh deformation [29] by taking the translated patches as shape constraints. For the mesh of skin with n vertices $V = \{v_1, \dots, v_n\}$, the Laplacian coordinate $\boldsymbol{\delta}_i$ on v_i can be computed by

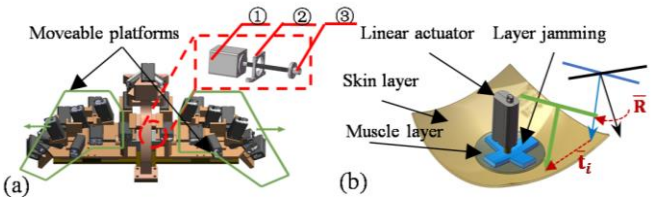

Figure. 6. Skeleton layer. (a) Moveable platforms, linear actuators and stepper motors of the skeleton layer. (b) The connection relationship between linear actuator, layer jamming bars, muscle layer and skin layer.

$$\boldsymbol{\delta}_i = \left(\delta_i^{(x)}, \delta_i^{(y)}, \delta_i^{(z)}\right) = L(v_i) = \mathbf{v}_i - \frac{1}{d_i}\sum_{j \in N(i)} \mathbf{v}_j \quad (12)$$

where $L(v_i)$ is the Laplacian operator on v_i, $N(i)$ is the adjacent vertice of v_i, and d_i is the number of its immediate neighbors. As constrained points, all the k vertices in each patch are translated to new positions $\mathbf{p}_i{}' = \mathbf{p}_i + d_i\mathbf{t}_i, i = 1, 2, \dots, k$, when the patch has been moved a distance d_i in the direction $\mathbf{t}_i$. Therefore, the deformation result can be obtained by solving

$$\min\left(\sum \|L(v_i') - \boldsymbol{\delta}_i'\|^2\right) \quad (13)$$
$$\text{s.t.}\{\alpha\mathbf{v}_l{}' + \beta\mathbf{v}_m{}' + \gamma\mathbf{v}_n{}' = \mathbf{p}_i + d_i\mathbf{t}_i, i = 1, 2, \dots, k\ \}$$

where $\boldsymbol{\delta}_i{}' = \mathbf{R}_i\boldsymbol{\delta}_i$, and $\mathbf{R}_i$ is the rotation matrix between the local region around v_i before and after deformation, which can be calculated with ASAP method [31]. As patches stick to the inner side of the skin layer, we parameterized the overlaps of two layers to enable that the shapes can be updated by each other during deformation. Each vertex p_i on the surfaces of the patches can be parameterized as $\mathbf{p}_i = \alpha\mathbf{v}_l + \beta\mathbf{v}_m + \gamma\mathbf{v}_n$, $\alpha + \beta + \gamma = 1$, where $\{\boldsymbol{v}_l, \boldsymbol{v}_m, \boldsymbol{v}_n\}$ are the three vertices of the relative triangle on the skin surface, (α, β, γ) is the barycentric coordinate of p_i, Similarly, each vertex on the skin layer contacting with a patch can be parameterized on the relative patch.

B. Deforming patches physically

After the Laplacian deformation of the skin, we calculated the stress distribution from the deformed mesh and the initial mesh, and then apply the stress to the corresponding nodes to start the finite element analysis. The elastic energy of deformed mesh can be computed as

$$E_{\text{elas}} = \sum\nolimits_{\Omega_i \in \mathcal{S}'} \Psi_i \,\text{vol}(\ t_i) \quad (14)$$

where the energy density Ψ is defined in (1) and $\text{vol}(\ \Omega_i)$ is the volume of the undeformed tetrahedron t_i. The elastic force on kth vertice contributed by tetrahedron t_i can be derived from the elastic energy as

$$\mathbf{f}_k^i = -\partial E_i(\boldsymbol{x})/\partial\overrightarrow{x_k} = -\frac{\text{vol}(\ t_i)\cdot\partial\Psi(\mathbf{F}_i)}{\partial\overrightarrow{x_k}} \quad (15)$$

Consequently, the elastic forces on four vertices can be collectively computed as

$$\mathbf{H} = [\mathbf{f}_1\ \ \mathbf{f}_2\ \ \mathbf{f}_3] = -W\mathbf{P}(\mathbf{F})\mathbf{D}_m^{-T},\ \ \mathbf{f}_4 = -\mathbf{f}_1 - \mathbf{f}_2 - \mathbf{f}_3 \quad (16)$$

where W is undeformed volume of the tetrahedron. $\mathbf{P}(\mathbf{F})$ is

$$\mathbf{P} = \frac{\partial \Psi(\mathbf{F})}{\partial \mathbf{F}} = \mu \mathbf{F} - \mu \mathbf{F}^{-T} \tag{17}$$

$\mathbf{D}_m$ is the undeformed shape matrix of each tetrahedron. It's defined as

$$\mathbf{D}_m \coloneqq \begin{bmatrix} X_1 - X_4 & X_2 - X_4 & X_3 - X_4 \\ Y_1 - Y_4 & Y_2 - Y_4 & Y_3 - Y_4 \\ Z_1 - Z_4 & Z_2 - Z_4 & Z_3 - Z_4 \end{bmatrix} \tag{18}$$

By accumulating of the contributions of all elements in its adjacent neighborhood N_i , the actual elastic force $\mathbf{f}_i$ on a node can be obtained as

$$\mathbf{f}_i(\vec{X}) = \sum_{e \epsilon N_i} \mathbf{f}_i^e(\vec{X}) \tag{19}$$

As the patches contact the skin continuously, the patches of the muscle layer are deformed by applying the inverse forces of $\mathbf{f}_i$ to the overlapping regions between the patches and the skin layer.

C. *Updating skin shape*

After updating the deformation of patches in Section III.B, the shape of the skin layer also needs to be recomputed. For the skin regions in contact with patches, their shapes are updated by the barycentric coordinates as described in Section III.A. For the skin regions between adjacent patches, the deformation is computed by minimizing the elastic energy with constraints of deformed patches. The elastic potential energy over all the elements E_{elas} is minimized to obtain the $\mathbf{F}_i$ as

$$\min \sum\nolimits_{\Omega_i \in \mathcal{S}'} \Psi_i(\mathbf{F}_i)\, \text{vol}(\ \Omega_i) \tag{20}$$

After updating the shape of the skin layer, a new iteration is started. We first recompute the deformation of patches and then recalculate the deformation of skin. The iteration processing is repeated until the biggest Hausdorff distance between the skin surfaces of two adjacent iterations is below the given threshold.

IV. Experimental Results

A physical robotic shoulder prototype has been built to verify the effectiveness of the layered structure.

Three-point bending tests has been carried out to verify the ability of our forked-finger layer jamming structure in adjusting stiffness, as shown in Fig. 7(a). The change in stiffness is measured by the deflection under different loads. As shown in Fig. 7(b). the air control system can adjust the stiffness of the forked-finger layer jamming by controlling the air pressure. The maximum output pressure of the pump is 0.8Mpa. The pressure regulator can control the work pressure in real time and convert the positive pressure into vacuum pressure. The valves have a plurality of air pipe interfaces, and the controller controls the on-off of each interface. The layer jamming structure has different mechanical curves under different pressure, as shown in Fig. 7(c). The greater the negative pressure, the higher the stiffness of the structure. When we applied vacuum pressure of -80kPa, the stiffness of the structure increased 94 times in 2s with 15 layers of filler.

The shape details of the shoulders can be imitated, such as shoulder width, arm circumference, shoulder slope, as shown in Fig. 7(d). By flexibly adjusting these body dimension parameters, the four common shoulder shapes, flat shoulder, sloping shoulder, broad shoulder, and narrow shoulder [32] can be imitated.

Quantitative evaluating experiments have been conducted to verify the shape imitating effects of our robotic shoulder. We selected three 3D models with different body shapes, and deformed our robotic mannequin shoulder to imitate them, as shown in Fig. 7(e), Fig. 7(f) and Fig. 7(g), respectively. Artec EVA 3D scanner is used to reconstruct the deformation results. The reconstruction rate is 16 frames/sec and the 3D resolution is 0.5mm. The reconstructed models are then aligned onto the target models by ICP (Iterative Closest Point) algorithm, and the shape errors between these two kinds of models are measured by Hausdorff distance, which are visualized as shown in Fig. 7(e), Fig. 7(f) and Fig. 7(g). Based on the results, the robotic shoulder has a better imitating effect on the chest, shoulder and back compared with the neck and arm. The largest errors occurred in the axillary and lateral thoracic regions, because of the lack of the actuator under the armpit and edge constraints on the skin layer.

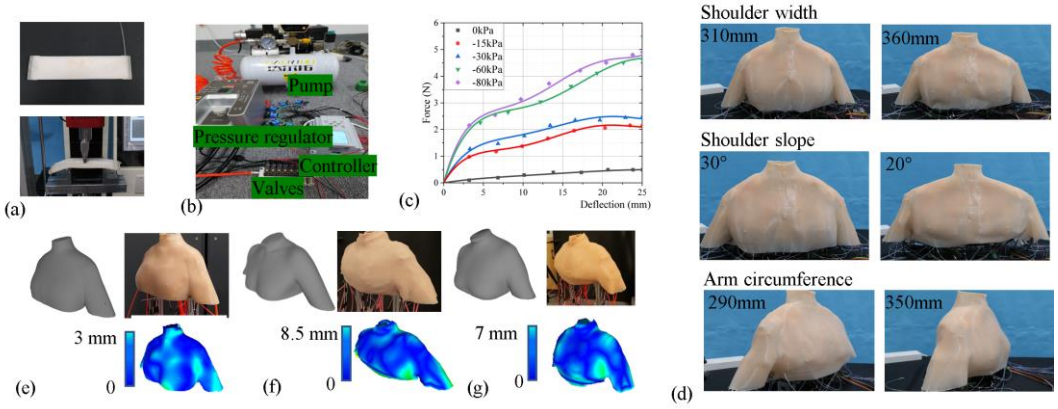

Figure. 7. Experimental results. (a) Layer jamming prototype and three-point bending experiment. (b) Air control system of layer jamming. (c) Experimental results of three-point bending of forked-finger layer jamming structure (d). The shape and size of the shoulders and arms imitated. (f), (g), and (h) Imitation of the target human models.

V. Conclusion

In this paper, inspired by human anatomy, we propose a novel three-layered robotic mannequin shoulder. From the inner to the outer, there are rigid skeleton layer consisting of linear actuators, flexible muscle layer composed of stiffness adjustable patches, and soft skin layer made of elastic silicone, respectively. The coupled three layers cooperatively shape the appearance of the robotic mannequin, enabling the robot to imitate body dimensions, local shape details and surface curvatures of different human bodies. An energy-based method for predicting such coupling deformation is proposed. Our approach explores a new way to design a physical shape-changing robot by coupling deformation of rigid, flexible and soft materials. The robotic mannequin shoulder prototype proposed in this paper have verified the imitating ability of our approach. We are considering extending the design of the robotic shoulder to a whole-body robotic mannequin.

Acknowledgment

This work was supported in part by National Natural Science Foundation of China 52275276 and in part by Research Funding of Zhejiang University Robotics Institute.

References

[1] A. Abels and M. Kruusmaa, “Design of a shape-changing anthropomorphic mannequin for tailoring applications,” p. 6.

[2] S. Peng, “Development of an interactive robotic mannequin for fashion industry,” 2013, Accessed: Jun. 19, 2022. [Online].

[3] J. Li, J. Weng, H. Xu, C. Zhou, D. Zhang, and G. Lu, “Design of robotic mannequin formed by flexible belt net,” *Computer-Aided Design*, vol. 110, pp. 1–10, May 2019, doi: 10.1016/j.cad.2018.12.010.

[4] Y. Tian, G. Fang, J. S. Petrulis, A. Weightman, and C. C. L. Wang, “Soft Robotic Mannequin: Design and Algorithm for Deformation Control,” *IEEE/ASME Transactions on Mechatronics*, pp. 1–10, 2022, doi: 10.1109/TMECH.2022.3175759.

[5] Z. Guo, D. Zhang, S. Zhang, X. Liu, and J. Li, “The design of a form-changing female fitting robot,” *JAMDSM*, vol. 10, no. 8, pp. JAMDSM0097–JAMDSM0097, 2016.

[6] “SIST EN 13402-2:2002 - Size designation of clothes - Part 2: Primary and secondary dimensions,” iTeh Standards. Accessed: May 21, 2023. [Online]. Available: https://standards.iteh.ai/catalog/standards/sist/9c72d228-0ad5-4e7f-9ad3-7b6fc3997bfc/sist-en-13402-2-2002

[7] Y.-T. T. Lee, “Body Dimensions for Apparel,” *NIST*, Jan. 1994, Accessed: May 21, 2023. [Online]. Available: https://www.nist.gov/publications/body-dimensions-apparel

[8] “Anthropometric definitions and methods for garment|GB/T 16160-2017.” Accessed: May 21, 2023. [Online]. Available: https://openstd.samr.gov.cn/bzgk/gb/newGbInfo?hcno=E703AB1DBE97906BF685F391700AC9E1

[9] “Eminéo and Miméo – Euveka’s connected solution – Euveka.” Accessed: Jun. 19, 2022. [Online]. Available: https://www.euveka.com/en/

[10] S. Lu, P. Y. Mok, and X. Jin, “A new design concept: 3D to 2D textile pattern design for garments,” *Computer-Aided Design*, vol. 89, pp. 35–49, Aug. 2017, doi: 10.1016/j.cad.2017.03.002.

[11] J. Li and G. Lu, “Modeling 3D garments by examples,” *Computer-Aided Design*, vol. 49, pp. 28–41, Apr. 2014.

[12] YangShan *et al.*, “Physics-Inspired Garment Recovery from a Single-View Image,” *ACM Transactions on Graphics (TOG)*, Nov. 2018, doi: 10.1145/3026479.

[13] H. Xu, J. Li, G. Lu, H. Deng, D. Zhang, and J. Ye, “Modeling 3D human body with a smart vest,” *Computers & Graphics*, vol. 75, pp. 44–58, Oct. 2018, doi: 10.1016/j.cag.2018.07.005.

[14] J. Huang, T.-H. Kwok, and C. Zhou, “Parametric design for human body modeling by wireframe-assisted deep learning,” *Computer-Aided Design*, vol. 108, pp. 19–29, Mar. 2019, doi: 10.1016/j.cad.2018.10.004.

[15] J. Li and G. Lu, “Customizing 3D garments based on volumetric deformation,” *Computers in Industry*, vol. 62, no. 7, pp. 693–707, Sep. 2011, doi: 10.1016/j.compind.2011.04.002.

[16] J. Li, J. Ye, Y. Wang, L. Bai, and G. Lu, “Fitting 3D garment models onto individual human models,” *Computers & Graphics*, vol. 34, no. 6, pp. 742–755, Dec. 2010, doi: 10.1016/j.cag.2010.07.008.

[17] N. Wu, Z. Deng, Y. Huang, C. Liu, D. Zhang, and X. Jin, “A fast garment fitting algorithm using skeleton-based error metric: Skeleton-Based Garment Fitting,” *Comput Anim Virtual Worlds*, vol. 29, no. 3–4, p. e1811, May 2018, doi: 10.1002/cav.1811.

[18] A. Kanazawa, M. J. Black, D. W. Jacobs, and J. Malik, “End-to-end Recovery of Human Shape and Pose.” arXiv, Jun. 23, 2018. Accessed: Jan. 03, 2023. [Online].

[19] T. Alldieck, M. Magnor, W. Xu, C. Theobalt, and G. Pons-Moll, “Video Based Reconstruction of 3D People Models.” arXiv, Apr. 16, 2018. Accessed: Jan. 03, 2023. [Online].

[20] Z. Zheng, T. Yu, Y. Wei, Q. Dai, and Y. Liu, “DeepHuman: 3D Human Reconstruction from a Single Image.” arXiv, Mar. 28, 2019. Accessed: Jan. 03, 2023. [Online].

[21] S. Saito, Z. Huang, R. Natsume, S. Morishima, A. Kanazawa, and H. Li, “PIFu: Pixel-Aligned Implicit Function for High-Resolution Clothed Human Digitization.” arXiv, Dec. 03, 2019. doi: 10.48550/arXiv.1905.05172.

[22] S. Yang, J. Liang, and M. C. Lin, “Learning-Based Cloth Material Recovery from Video,” in *2017 IEEE International Conference on Computer Vision (ICCV)*, Venice: IEEE, Oct. 2017, pp. 4393–4403.

[23] Y.-L. Qiao, J. Liang, V. Koltun, and M. C. Lin, “Scalable Differentiable Physics for Learning and Control.” arXiv, Jul. 04, 2020. doi: 10.48550/arXiv.2007.02168.

[24] L. Pishchulin, S. Wuhrer, T. Helten, C. Theobalt, and B. Schiele, “Building Statistical Shape Spaces for 3D Human Modeling,” *Pattern Recognition*, vol. 67, pp. 276–286, Jul. 2017.

[25] H. Si, “TetGen, a Delaunay-Based Quality Tetrahedral Mesh Generator,” *ACM Trans. Math. Softw.*, vol. 41, no. 2, pp. 1–36, Feb. 2015, doi: 10.1145/2629697.

[26] L. Marechal, P. Balland, L. Lindenroth, F. Petrou, C. Kontovounisios, and F. Bello, “Toward a Common Framework and Database of Materials for Soft Robotics,” *Soft Robotics*, vol. 8, no. 3, Art. no. 3, Jun. 2021, doi: 10.1089/soro.2019.0115.

[27] G. H. Golub and C. Reinsch, “Singular value decomposition and least squares solutions,” p. 18.

[28] “GB 10000-1988 English Version, GB 10000-1988 Human dimensions of Chinese adults (English Version) - Code of China.” Accessed: Jul. 22, 2022. [Online]. Available: https://www.codeofchina.com/standard/GB10000-1988.html

[29] O. Sorkine, D. Cohen-Or, Y. Lipman, M. Alexa, C. Rössl, and H.-P. Seidel, “Laplacian surface editing,” in *Proceedings of the 2004 Eurographics/ACM SIGGRAPH symposium on Geometry processing - SGP '04*, Nice, France: ACM Press, 2004, p. 175.

[30] E. D. Sifakis, “FEM Simulation of 3D Deformable Solids: A practitioner’s guide to theory, discretization and model reduction. Part One: The classical FEM method and discretization methodology,” *ACM SIGGRAPH 2012*, p. 35.

[31] O. Sorkine and M. Alexa, “As-Rigid-As-Possible Surface Modeling,” p. 8.

[32] L. Ran *et al.*, “Study of Body Shoulder Shaping for Chinese Females Based on 3-D Body Measurement,” in *Advances in Manufacturing, Production Management and Process Control*, W. Karwowski, S. Trzcielinski, B. Mrugalska, M. Di Nicolantonio, and E. Rossi, Eds., in Advances in Intelligent Systems and Computing. Cham: Springer International Publishing, 2019, pp. 307–313.